Optimizing a SiC-based Nuclear Instrumentation System for Molten Salt Reactors

Kevin Kelly,[a] and Bojan Petrovic[*,a]

[a] *Georgia Institute of Technology*
770 State St NW, Atlanta, GA 30313

[*]Email: bojan.petrovic@gatech.edu

Number of pages:	34
Number of tables:	8
Number of figures:	33

Abstract

Silicon Carbide based radiation detectors have an exceptional capacity to perform in harsher radiation environments due to favorable thermal properties and stability through high fluences. In combination with the capability to accurately measure thermal and fast neutrons and discriminate from gamma-rays, SiC becomes an obvious candidate for nuclear instrumentation in advanced reactor designs. To effectively put this technology into practice, a detection system will be evaluated against several parameters to ensure an adequate signal is available and detector performance is maintained over a desired lifetime. Weighting factors for detector location, shielding, and size are developed so that the work may be extrapolated to other projects.

Keywords — Molten Salt Reactor, SCALE, OpenMC, Silicon Carbide Detector, Power Monitoring

I. INTRODUCTION

An increased design focus on small reactor models in the nuclear industry combined with advancements in detection technologies presents an opportunity to explore alternative instrumentation solutions. Traditional systems monitor power from shutdown conditions to excursions at 200% full power. The span of fluxes is typically subdivided into Source, Intermediate, and Power ranges and each range is handled with a different detector based on respective limitations in response time and neutron signal discrimination. [1,2] From an Operations and Maintenance perspective, it may make sense to reduce the complexity to a single type of detector if feasible. This has previously been demonstrated using Silicon Carbide (SiC) detectors at Cornell's TRIGA research reactor [3], considered for the IRIS[4] and I²S-LWR [5,6] reactor concepts, and may be of interest to the planned Molten Salt Research Reactor (MSRR) project at Abilene Christian University (ACU) [7]. This study therefore seeks to explore SiC detection capabilities and limitations in the context of a simplified Molten Salt Reactor (MSR).

I.A. Molten Salt Reactors

Interest in Molten Salt Reactors began in the late 1940's in pursuit of a nuclear powered aircraft for the United States and has since resurfaced as one of the Generation IV reactor technologies chosen for further research and development. [8][9] The 2.5 MW Aircraft Reactor Experiment in 1954 and subsequent 8MW Molten Salt Reactor Experiment (MSRE) in 1960 at Oak Ridge successfully demonstrated the design and serve as a foundational source of experimental data for new designs. [8] The MSRE operated until 1969 using a lithium fluoride and beryllium fluoride (FLiBe) fuel salt mixed with ZrF_4 and either ThF_4 with UF_4, highly-enriched UF_4 or partially enriched UF_4. [10] The fuel salt flowed through a graphite-moderated core, where it reached an outlet temperature of about 935 K, transferred heat to a secondary coolant salt, and then radiated the heat to the atmosphere. [10] Due to the harsh environment inside the reactor core, most neutron measurement will occur outside of the core. This study will focus on full-range power level change measurements. Requirements for various neutron measurement functions specific to MSRs are summarized in Table 1 of Reference [11].

I.B. Silicon Carbide Detectors

Silicon Carbide detectors, more specifically the alternating cubic and hexagonal 4-layer stacking sequence and hexagonally symmetric 4H-SiC, offer high temperature operation, radia-

TABLE I

Summary of Select 4H-SiC Properties

Density	(g/cc)	3.2
Band Gap	(eV)	3.27
Thermal Conductivity	(W/cmK)	4.9
e-h pair creation energy	(eV)	7.78
Displacement Energy	(eV)	30-40
electron mobility	(cm^2/Vs)	800
hole mobility	(cm^2/Vs)	115
Critical Electric Field Strength	(V/cm)	$2\text{-}5 \cdot 10^6$

tion resistance, fast response times, and neutron signal discrimination. [12, 13] A summary of selected properties is located in Table I. [3, 12, 14]

The wide band gap allows for low leakage currents at a high electric fields, which is important for a low signal to noise ratio. A relatively high thermal conductivity allows for better heat dissipation and thereby greater tolerance for high-temperature environments. As a consequence of the high band gap, the electron-hole pair generation energy is proportionally high, but only needs to be small enough to allow for sufficient charge generation at a given ionization energy. Radiation resistance is in part attributable to the relatively high displacement energy. The critical electric field strength depends on doping concentration of the detector and is the point at which the p-n junction will start to break down. Since SiC can support high electric fields, the velocity of the electrons and holes can saturate at about 200 µm/ns and allow for very fast response times in millimeter-scale detectors. [12]

In this study, a SiC detector will be modeled outside of a reactor core to function as a power monitoring system. Reactor power is proportional to the ex-core neutron flux and therefore a simulated signal to the detector based on particle interactions will serve as a basis for optimization.

II. METHODOLOGY AND RESULTS

The model used for analysis is a simplified version of the proposed Abeline Christian University Molten Salt Research Reactor. [7] The model was simulated using the SCALE 6.2.4 and OpenMC v0.13.2 code suites. SCALE is a widely adopted modeling and simulation suite developed and maintained by Oak Ridge National Lab. [15] Within SCALE, the Criticality Safety Analysis Sequence (CSAS), Transport Rigor Implemented Time-dependent Operation for Neutronic depletion (TRITON), and Monaco with Advanced Variance Reduction using Importance Calculations (MAVRIC) were utilized to characterize the radiation environ-

ment over the cores lifetime and estimate a detectors response. OpenMC is an open source Monte Carlo code developed by members of the Computational Reactor Physics Group at the Massachusetts Institute of Technology and will primarily be used for data validation, but includes a Python API that allows for simple data processing. [16] Further discussion of each code package will be provided in the respective section they are used. An overview of the approach in SCALE is provided in Figure 1.

II.A. Materials

The materials used in the model are listed in Table II. The identifier corresponds to the labeled instance of the material in Figure 2. Densities are nominal, except for the boron carbide which is at 75% theoretical density. Thermodynamic properties are kept constant across the core since the objective is to understand the magnitude of the radiation environment rather than attempt to accurately predict criticality, power shape, or other parameters which would rely on more subtle changes in such properties.

II.B. Geometry

The modeled reactor vessel consists of 87 fuel salt channels in a hexagonal lattice of graphite of equivalent dimension to the MSRR, but without control rods or their channels. The

graphite block is a standard cylinder rather than spherically tapered at each end, resulting in a greater volume of fuel salt above and below the core in this model. Finally, a thin annulus of fuel salt exists around the graphite lattice where it then meets the steel reactor vessel. Primary and secondary systems outside of the core have been omitted. The reactor vessel is progressively surrounded by a polyethylene and boron carbide internal shield, stainless steel reactor enclosure, borated concrete shielding, and lastly, the structural concrete. A side profile of the reactor is shown in Figure 2, with a top-down view of the core in Figure 3.
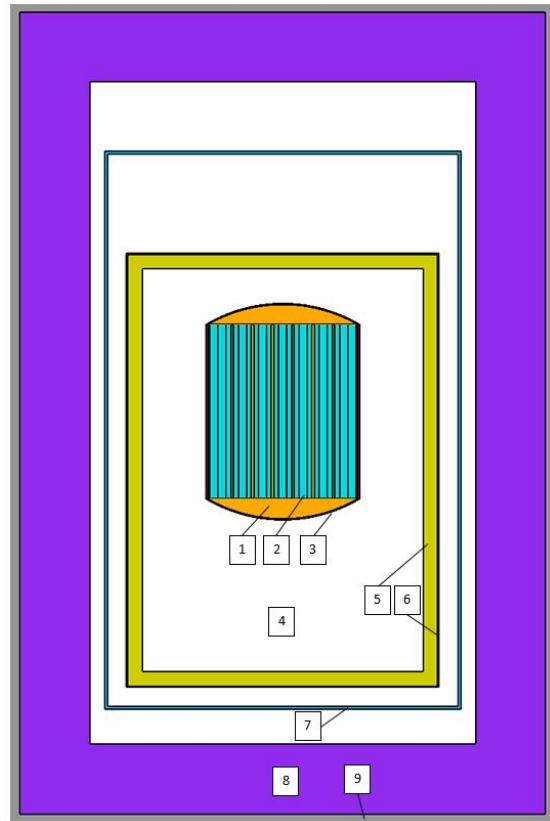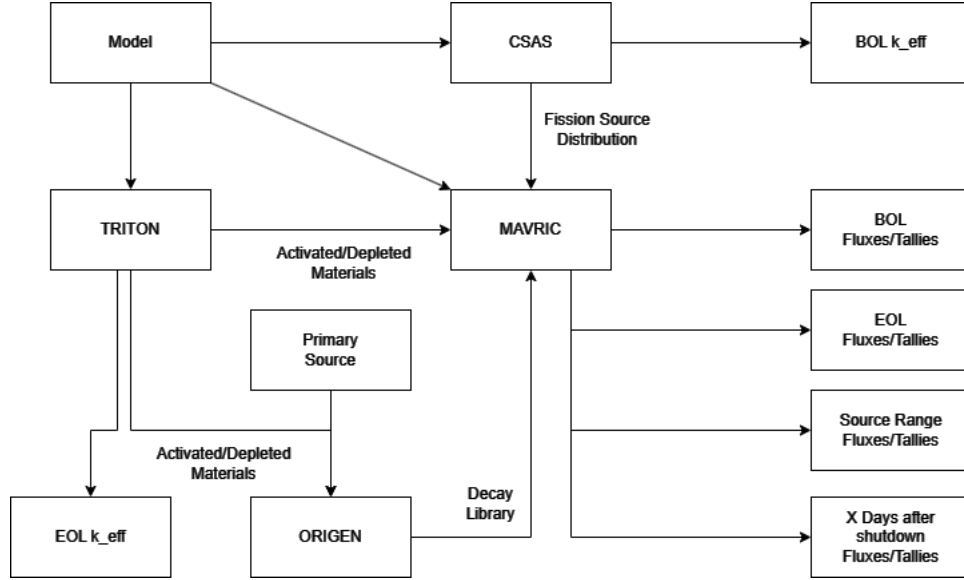

Fig. 2. Side View of Model Core at Midplane

5

Fig. 1. SCALE Methodology Diagram

TABLE II
Summary of Materials

ID	Component	Composition	Density (g/cc)	Temperature (K)
1	Fuel Salt	FLiBe (67.2%LiF-27.8% BeF2-5.0%UF4)	2.645	873
2	Moderator	Graphite [17]	1.8	873
3	Reactor Vessel	SS316H [17]	8.0	873
4	Air Gap	Air [17]	0.00129	300
5	Internal Shield	Polyethylene [17]	0.94	300
6	Internal Shield	Boron Carbide [17]	1.89	300
7	Reactor Enclosure	SS316H [17]	8.0	300
8	Concrete Shielding	M1 Concrete [17]	4.5	300
9	Structural Concrete	Oak Ridge Concrete [17]	2.3	300
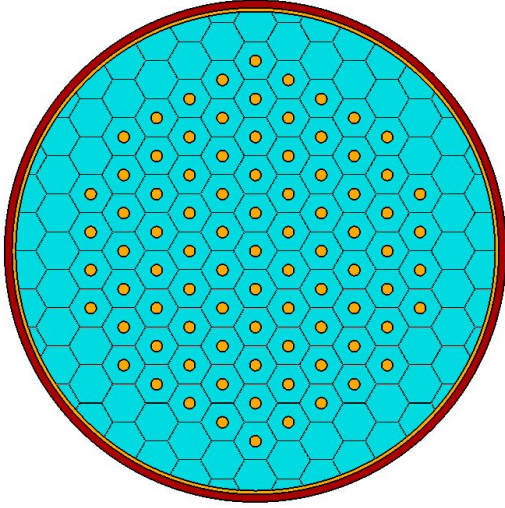
Fig. 3. Top-down View of Model Core at Mid-plane

II.C.   Radiation Environment

Eigenvalue calculations were performed using the KENO VI Monte Carlo transport simulation within CSAS and using the 'k-eigenvalue' setting in OpenMC. Beginning Of Life (BOL) k-effective, its error and simulation information are reported in Figure III. Clearly, the reactor cannot be run in a supercritical state, but the method of excess reactivity suppression is not yet definitive for the MSRR and the parameters of interest for detection are the fluxes calculated during the simulation.

Fluxes in KENO are computed across a mesh volume using a track length estimator and reported in neutrons per cm^2 per source particle (Equation 1). [15]

$$\Phi_{g,z} = \frac{\sum_{k=1}^{K} W_{k,z} I_{k,z}}{V_z \sum_{k=1}^{K} W_{k,0}} \qquad (1)$$

where: Particle, k, Region, z, Distance traversed, l, Volume, V, Weight, W, Total number of particle histories, K.

By multiplying this scalar flux by a normalizing factor, flux can be achieved in the more practical form of neutrons per cm^2 per second. OpenMC, however, originally reports in neutron-cm per source particle and must therefore also be divided by volume to normalize. These values can be validated across codes by utilizing a feature of TRITON in SCALE whereby total flux is reported at each depletion step, averaged across the volume of a material. OpenMC allows fluxes to be tallied across materials and can then be normalized using Equation 2 and the total material volume. Converting from a material tally to a mesh tally in OpenMC, the OpenMC tally can be seen to differ from the SCALE mesh of the same dimensions by the volume of the voxel used. This is shown explicitly in Table IV. Item 1 is calculated by hand. Item 2 is derived from Item 1, a 1 MW thermal power and the Fuel Salt composition in Table II. Item 3 is the total flux averaged across the Fuel Salt material volume. Item 5 is the OpenMC reported fission rate tallied over the Fuel Salt volume. Item 6 is Item 4 multiplied by Equation 2 and divided by Item 1. Item 7 and 8 are un-

TABLE III
BOL Criticality Simulation

	SCALE	OpenMC
Cross Section Library	ENDF/B-VII.1	ENDF/B-VII.1
# Generations	200	200
# Particles per Generation	150000	150000
# Skipped Generations	30	30
k_{eff}	1.03701	1.03693
Standard deviation	0.00019	0.00021

normalized track-length estimators of the flux in the center of the core for the Item 9 voxel size and are seen to differ roughly by a factor of 4 (2x2x1).

$$\frac{sourceparticles}{second} = \frac{P\bar{\nu}}{Qk} \qquad (2)$$

where: Power (J/s), P, Average fission neutron yield (n/fission), $\bar{\nu}$, Energy per fission (J/fission), Q, Neutron multiplication factor (n/source), k.

Normalized total fluxes from SCALE are shown in Figure 4, with relative uncertainties in Figure 5. Similar values can be seen resulting from OpenMC in Figure 6. 2-D radial flux plots along the core midplane are shown for the thermal (<0.0625 eV), epithermal (0.0625 eV to 1 MeV), and fast (>1 MeV) energy ranges Figure 7. No thermal neutrons are observed past the boron carbide Neutron Shield (136 cm) in these analog simulations.
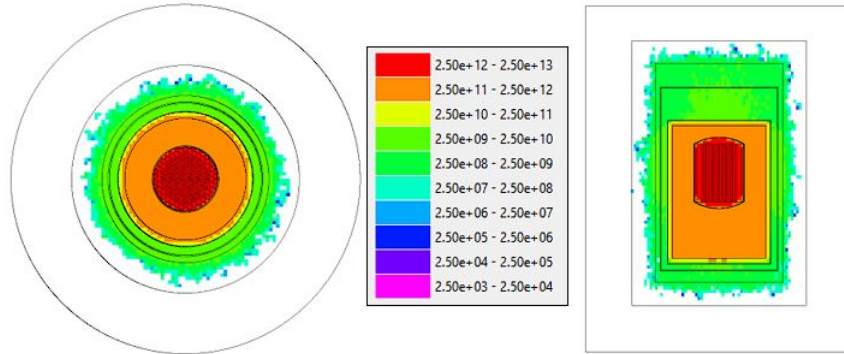

Fig. 4. Normalized total fluxes for SCALE in neutrons per cm^{2}s

TABLE IV
Validated Normalization

Item #	Item	Value
1	Fuel Volume	391291 cm^3
2	Specific Power	3.763 W/g
3	TRITON-Calculated Flux	4.95E+12 n/cm^2
4	OpenMC Material Tally	26.36 n-cm/source
5	Fission Rate	0.4245 fissions/source
6	OpenMC Normalized Flux	4.94E+12 n/cm^2
7	OpenMC Mesh Tally	1.33E-3 n-cm/source
8	SCALE Mesh Tally	3.39E-4 n/(cm^2*source)
9	Mesh Dimensions	2x2x1 cm
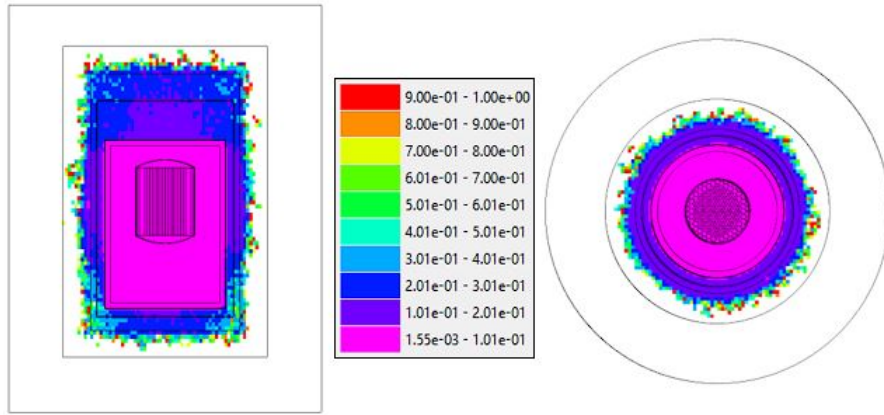
Fig. 5. Relative uncertainty in flux for SCALE
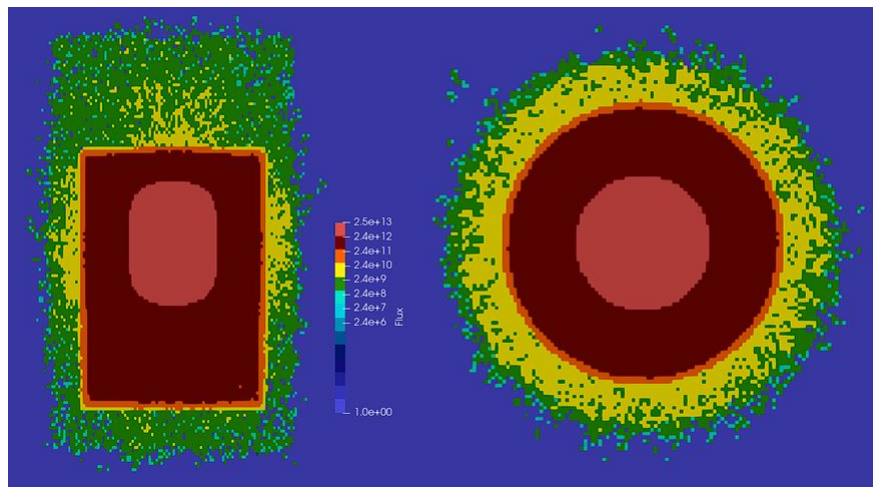
Fig. 6. Normalized total fluxes for OpenMC in neutrons per cm^{2}s
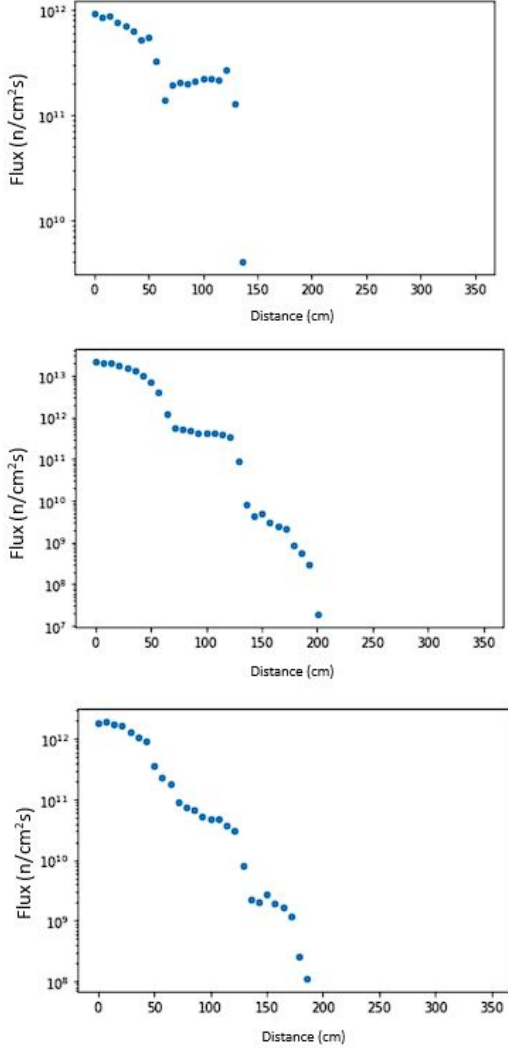
Fig. 7. Normalized thermal, epithermal, and fast (Top to Bottom) fluxes for OpenMC along the core midplane

II.D. Employing Variance Reduction

A limitation of obtaining fluxes directly from KENO is the significant run time associated with large numbers of particles, leading to either no data or large uncertainties at the periphery of the problem (Figure 5). Variance reduction in SCALE is accomplished using MAVRIC, which utilizes a combination of the DENOVO and MONACO packages. DENOVO performs a 3-D discrete-ordinates calculation to compute the adjoint or forward flux, which is used to create an importance map and biased source distribution for a particular response function Equation 3 to automatically weight particles when they are born and during transport Equation 4 [15].

$$\hat{q}(\vec{r}, E) = \frac{1}{R} q(\vec{r}, E)\phi^+(\vec{r}, E) \qquad (3)$$

$$\bar{w}(\vec{r}, E) = \frac{R}{\phi^+(\vec{r}, E)} \qquad (4)$$

where: Biased source distribution, $\hat{q}(\vec{r}, E)$, Total detector Response, R, Source emission probability distribution function , $q(\vec{r}, E)$, Adjoint scalar flux, $\phi^+(\vec{r}, E)$, Weight window target values, $\bar{w}(\vec{r}, E)$.

To instead bias the source across a volume, a separate forward S_N calculation is used to estimate expected tally results and inversely weight the source based on the estimation. Equation 3 becomes Equation 5, where when total flux is of interest, $\sigma_d E = 1$.

$$q^+(\vec{r}, E) = \frac{\sigma_d(E)g(\vec{r})}{\sigma_d(E)\phi(\vec{r}, E)dE'} \qquad (5)$$

10

where: Forward biased source distribution, $q^+(\vec{r}, E)$, Detector response function , $\sigma_d(E)g$, Spatial location, $g(\vec{r})$, Forward flux estimate, $\phi(\vec{r}, E)$.

The first step in the process is to obtain the fission source distribution from CSAS. Running 200000 particles per generation for 500 generations for a 200x200x200 mesh achieves Figure 8 and Figure 9 in about 30 hours of serial run-time. This fission source distribution was then imported into MAVRIC with a normalized strength of 7.34E16 source particles per second. The run used Legendre expansion P_1 and S_4 quadrature, with "fluxweighting" in the importanceMap block for a forward biased source distribution to obtain fluxes for the whole geometry. The run of 2 billion total particles using the 27n19g cross section library took approx. 42 hours in serial to produce Figure 10 and Figure 12. Figure 11 is from the same run, but focuses on the flux distribution within the core.

II.E. Depletion

As fissile material is burned, the total neutron flux required to obtain a certain power level in the core will change over time. To accurately bound the magnitude of the radiation environment, it must be evaluated over the expected lifetime of the reactor. Depletion calculations are performed in 3-D using the TRITON mod-

ule in SCALE and using the CECM Integrator method in OpenMC. The solver used for both codes was the Chebyshev Rational Approximation Method (CRAM) [18, 19].

Several caveats must be discussed regarding the nature of the depletion; the first of which being the expected lifetime of the reactor. Since the Preliminary Safety Analysis Report [7] is the current extent of publicly available information, the research reactor's lifetime is assumed to be roughly the same as the MSRE. Without a confirmed refueling plan or known ex-core fuel volumes, it would seem both conservative and simple to assume the in-core volume is active at full power for a roughly five year period. For a calculated power density of 3.763 W/g, the reactor total burnup is relatively low and is not expected to have a huge impact on total fluxes. A simple burn to End Of Life is presented in Figure 13.

As a bounding assessment, attention is only given to the EOL state as the potential worst case flux scenario; the expectation being that greater fluxes are needed to maintain the same power level as fuel is depleted. It is noted that $\bar{\nu}$ has increased from ≈ 2.4389 at BOL to ≈ 2.4489 at EOL. The fission rate has also increased in the upper and lower plenums, likely attributable to the stationary nature of the salt during depletion leading to unrealistic breeding. This effect on flux is exaggerated at the upper
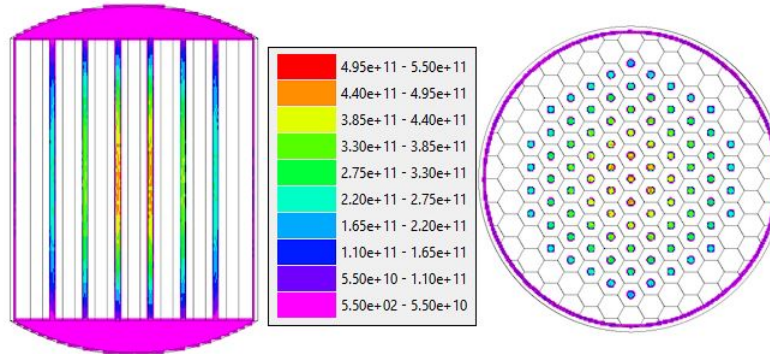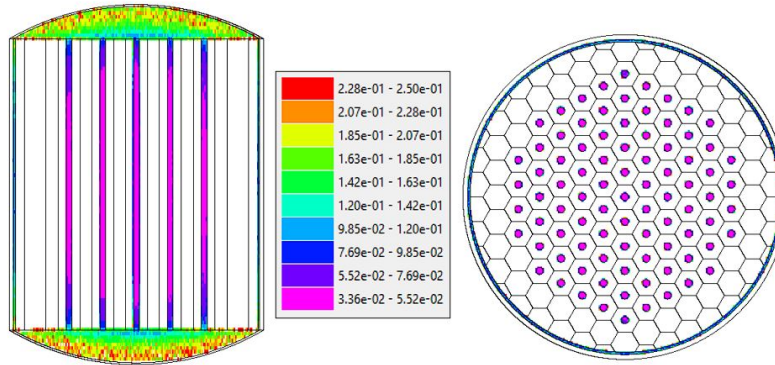
Fig. 8. Fission rate in fissions per cm^{3}s
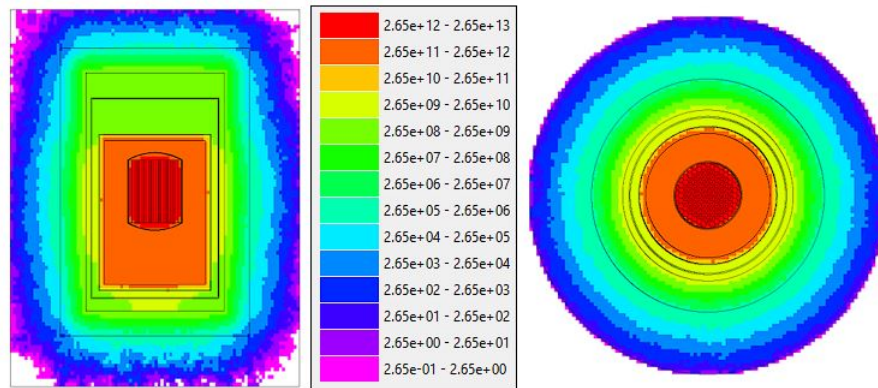

Fig. 9. Relative uncertainty in fission rate (0-25%)
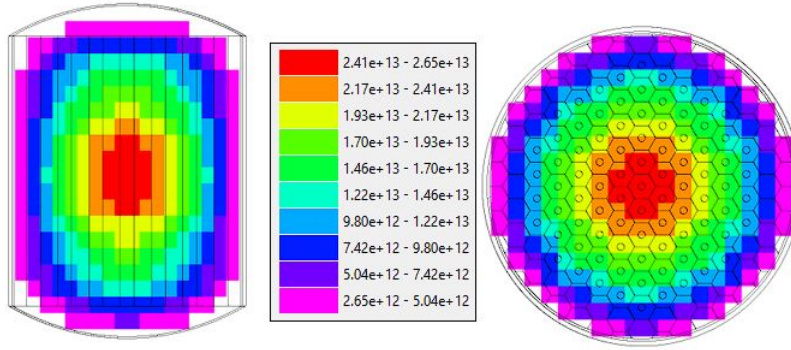

Fig. 10. Total flux in neutrons per cm^{2}s

12

Fig. 11. Total flux in-core in neutrons per cm²s

plenum due to proximity to the neutron shield, which additionally acts as a reflector in this scenario. Ultimately, fluxes are within about 20% of the values at BOL and the behavior observed above and below the core at EOL should be considered unreliable (Figure 14, Figure 15).
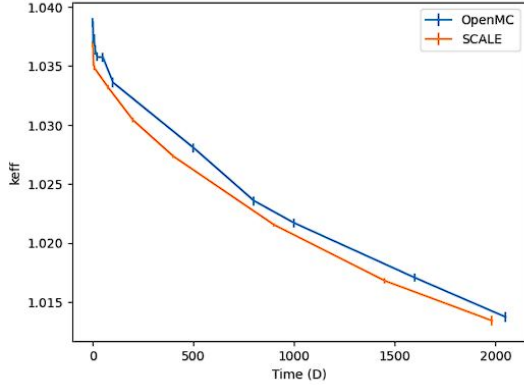

Fig. 13. Change in k_{eff} over reactor lifetime

II.F. Startup Source Detection and Activation Analysis

In order to function as a full-range power monitoring device, a detector must also be able to accurately measure the reactor system for startup conditions. Source range detection represents the lower bound of acceptable count rate for the detector, typically around 2 counts per second. After the reactor has accumulated fission products and activated materials through operation, significant gamma noise will be present in the detector environment. Discrimination between the gamma and neutron signal pulses is therefore a necessary requirement for the detection system to operate in the source range.

II.G. Primary Source

Since no information on start-up source implementation is available for the MSRR project, the core configuration is based on the primary source setup for a light water reactor design [20]. The base core was modified to contain two Cf-252 sources and one Gadolinium control channel in place of 3 of the fuel salt channels to create a superficial sub-critical system as shown
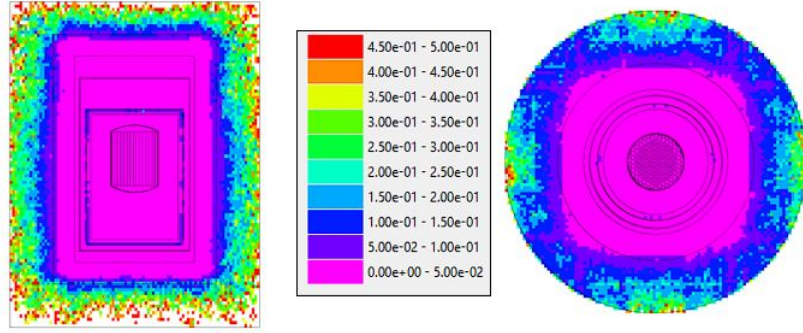
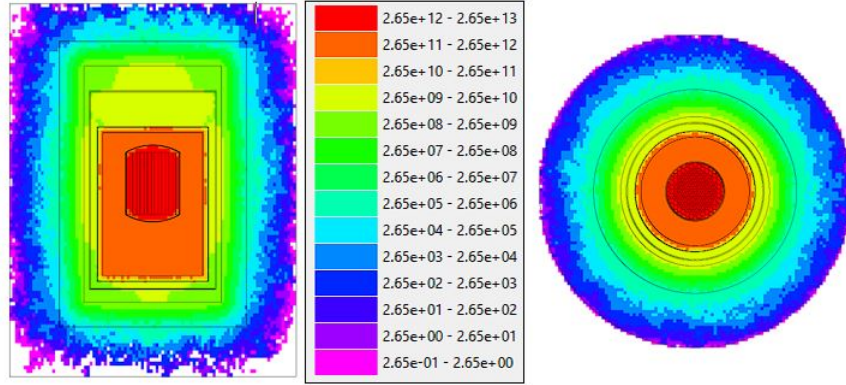Fig. 12. Relative uncertainty in total flux

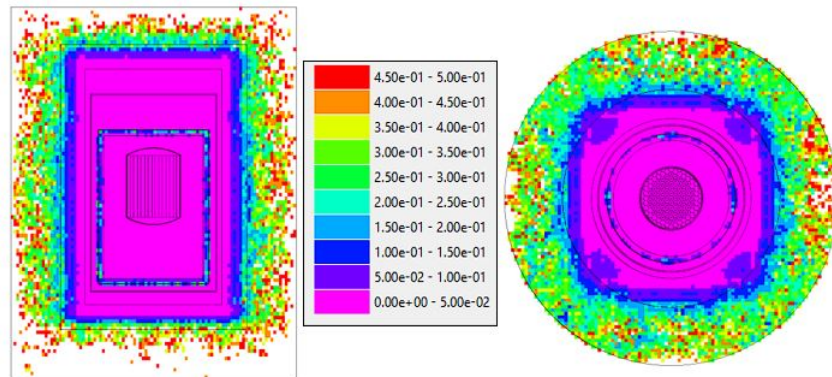Fig. 14. EOL total flux in neutrons per cm^{2}s

Fig. 15. Uncertainty in EOL total flux

14

in Figure 16. The initial mass of Cf-252 present in the core is of equivalent ratio of mass of Cf-252 to mass of U-235 for the light water reactor scenario. The Cf-252 is placed in the center of the fuel channel, with steel filling the channel above and below to represent an arbitrary support structure. More specific data regarding the source configuration is located in Table V. Parameters a and b are used to approximate the energy distribution of Cf using the Watt spectrum of the form shown in Equation 6.

$$p(E) = ce^{\text{-E/a}}sinh(\sqrt{bE}) \tag{6}$$

where: Fission probability, p(E), Isotope specific parameters related to average fission energy, a and b, Normalization constant to ensure cumulative probability of 1, c, Energy, E.
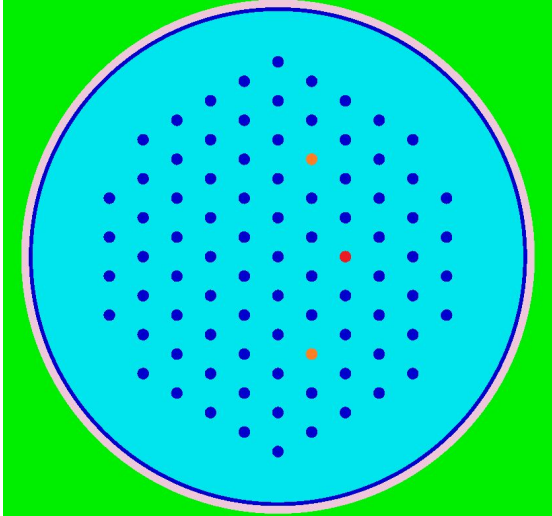

Fig. 16. Start-up source configuration. 2 primary sources shown in orange with the Gd channel in red.

II.H.   Activation Analysis

The final bounding assessment pertains to activation of non-fuel materials, particularly the reactor pressure vessel and the neutron shield. During the reactor lifetime, the primary source will also decay over time, leading to a lower strength available to detect. The fuel depletion, and activation of the neutron shield and reactor pressure vessel was done in the TRITON sequence, while the Cf source was done in ORIGEN using fluxes from TRITON at equivalent time steps. Downtime after operation was simulated using the end7dec library at 30 and 180 days to obtain a general idea of how an outage may affect radiation levels. Under shutdown and low-power conditions, the gamma radiation emitted by the materials is non-negligible and the detector must be able to discriminate between incident energy from the source, fuel and noise.

Denovo is not capable of modeling multiplying media, so the flux is approximated using MAVRIC in a non-multiplying mode (fissionMult=0) and the sub-critical multiplication factor (Equation 7), using k_{eff} from Table V.

$$M = \frac{1}{1 - k_{\text{eff}}} \tag{7}$$

where: Multiplication factor, M

Figure 17-Figure 20 show total neutron

TABLE V

Startup source configuration properties

Source Configuration	
Cf Volume	0.04 cm^3
Cf Density	15.1 g/cm^3
Source Strength	1.4496E+12 n/s
Axial Source Locations	Channel midpoint
Energy Distribution	Watt spectrum, a=1.025 MeV, b=2.926 1/MeV [15]
k$_{eff}$ evaluated via CSAS	0.95988 ± 0.00041

and photon flux, with their respective uncertainties, after 5 years of core operation. The 0 day case was run with 80 million particles while the 30 and 180 day case were run with 10 million. It can be observed that there are infrequent photons leading to flux values above 1E7 magnitude and corresponding 90% uncertainties. Neutron flux remains in the 1E8 magnitude between the core and neutron shield over the 180 day period, while photon flux largely remains between 3E5 and 4E6 - with significant noise in the data. This environment will be used for the "source range" detection scenario, which will be further discussed in III.F.

II.I. Detector Response

The detectors response is modeled in MAVRIC and OpenMC based initially on the dimensions of [21]. A series of cylinders of equivalent cross-sectional area to the normal 4.4mm x 4.4mm rectangular SiC wafers are used for simplification of modeling. The detector consists of an enriched LiF converter layer, fol-

lowed by a Ni Schottky diode, an active and inactive SiC detector volume (based on reverse bias), and a final Ni Ohmic contact (Figure 21). Neutron detectors rely on secondary effects of reactions to obtain the charged particles necessary for a detection event. SiC is intrinsically capable of fast neutron detection based on the ^{28}Si(n,p), ^{28}Si(n,α), ^{28}Si(n,n') and ^{12}C(n,α), ^{12}C(n,n') reactions, while lower energies rely on the Lithium-6 reaction shown in Equation 8.

Fig. 21. LiF (1.5 μm), Ni (0.8 μm), SiC (0.015 cm active, 0.035 cm inactive), Ni (0.8 μm) Not to scale.

$$^6Li + n \rightarrow\, ^4He +\, ^3H \qquad (8)$$
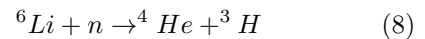
Since SCALE and OpenMC do not transport charged particles and currently lack a
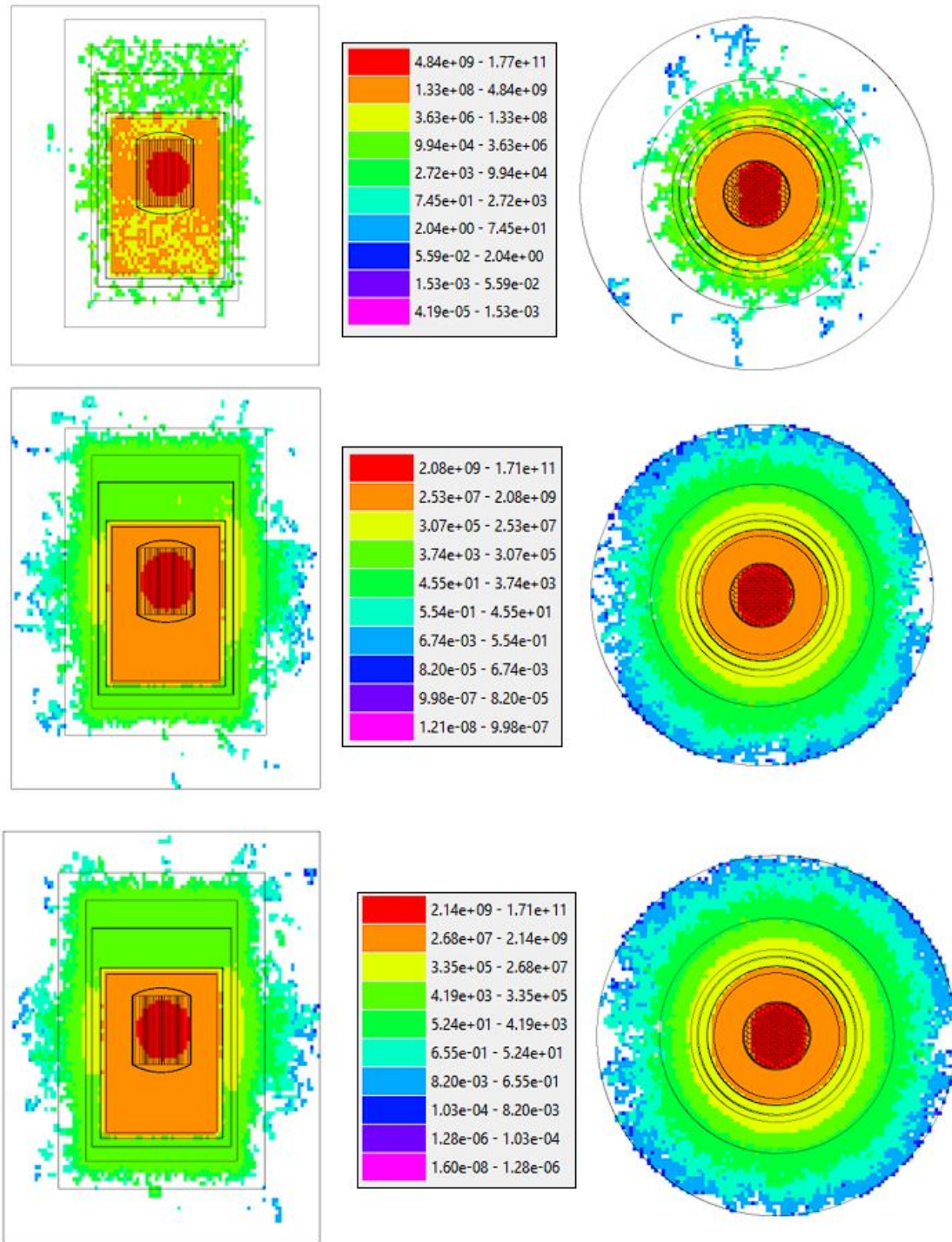
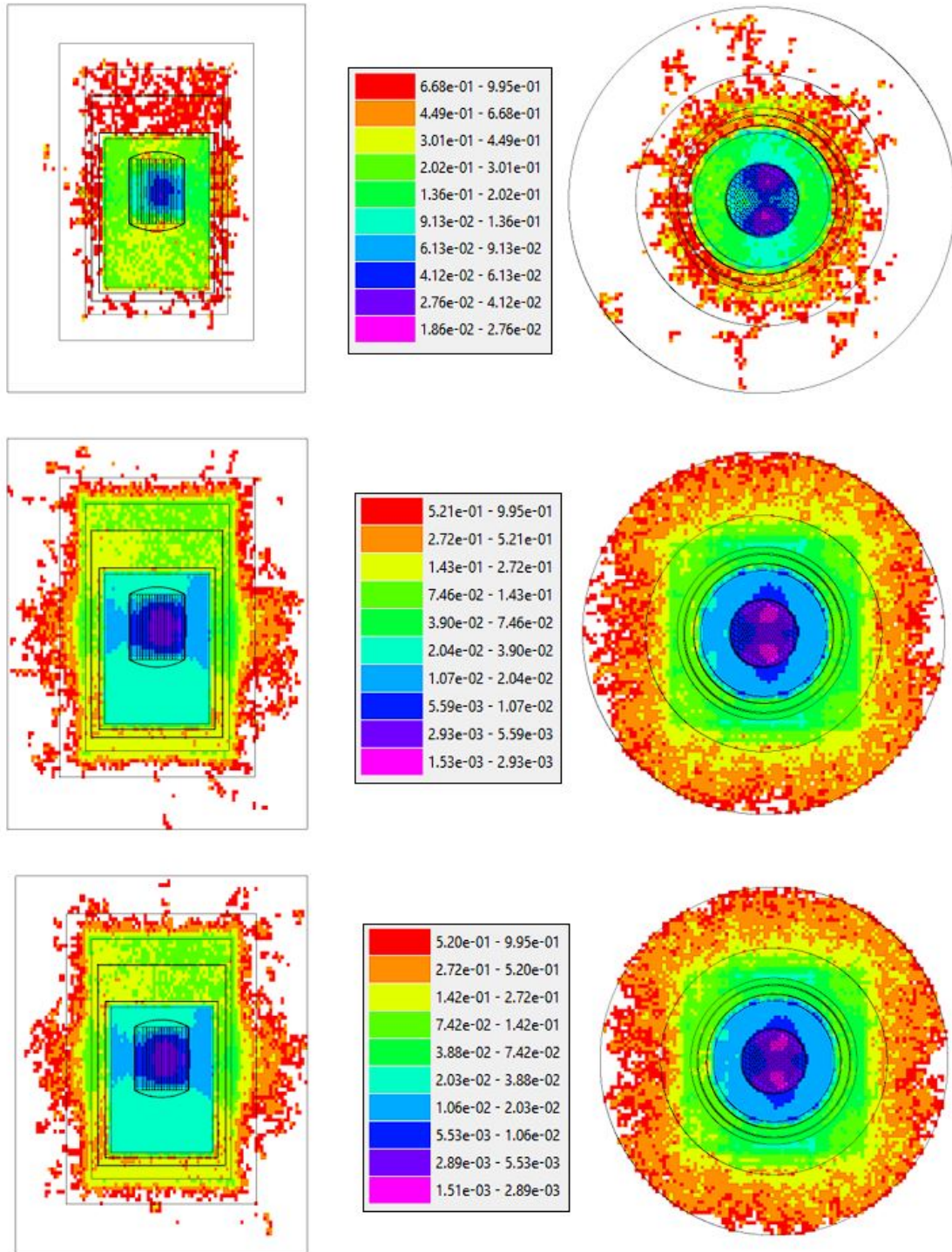Fig. 17. Total neutron flux per cm^{2}s after 5 years of operation and after 0, 30, and 180 days of shutdown (Top to bottom)

17

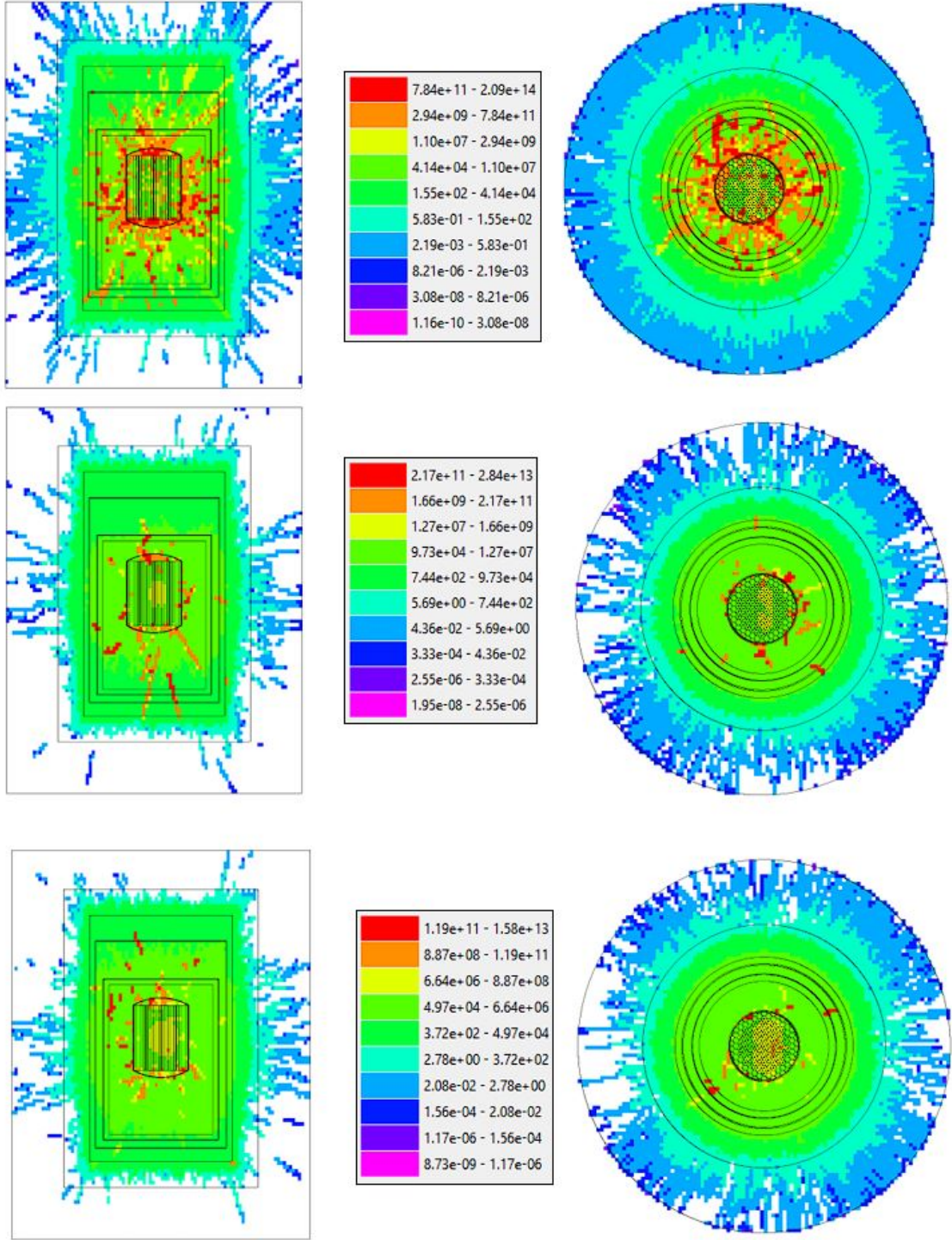Fig. 18. Uncertainty in total neutron flux per cm^{2}s after 5 years of operation and after 0, 30, and 180 days of shutdown (Top to bottom)

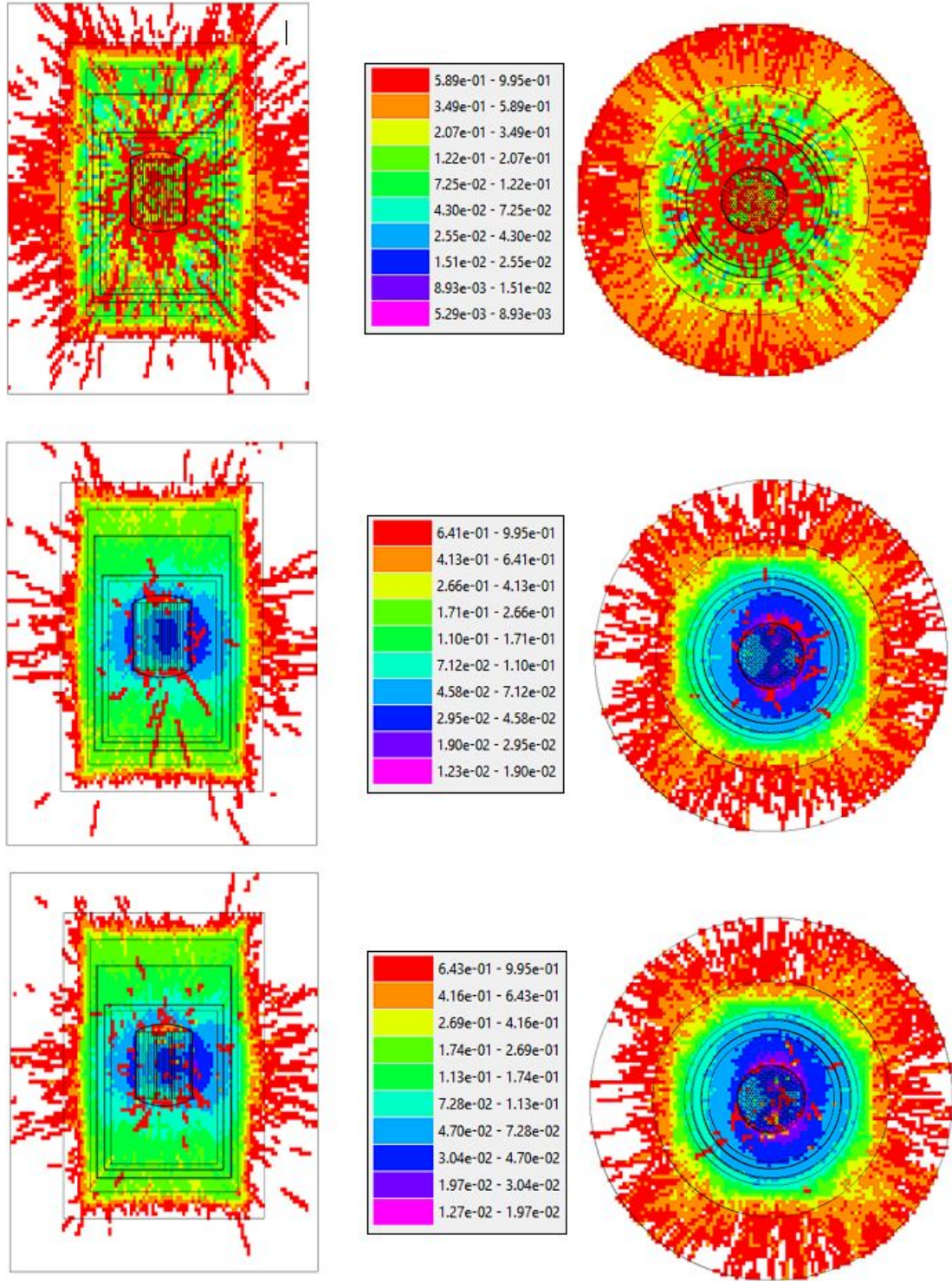Fig. 19. Total photon flux per cm^{2}s after 5 years of operation and after 0, 30, and 180 days of shutdown (Top to bottom)

Fig. 20. Uncertainty in total photon flux per cm^{2}s after 5 years of operation and after 0, 30, and 180 days of shutdown (Top to bottom)

"pulse height tally" (F8 in MCNP), the detector behavior is modeled using reaction based tallies [22] coupled with a custom Python script used to transport the charged particles generated in the LiF volume. For OpenMC, in the active SiC volume, a heating tally is used to include all direct energy deposition to the detector. In SCALE, absorption (MT=27) and total photon interaction (MT=501) are used to approximate the detector signal. A clear limitation of this approach is that only information of the incident energy is known, rather than the total energy deposited in the scenarios where scattered particles exit the detector volume. This, however, remains a useful metric for pulse shape discrimination since absorption corresponds to the maximum depositable energy for the interaction. Alpha and triton production is tallied in the LiF volume and an equivalent number of particles is simulated using the Python script using a Continuous Slowing Down Approximation (CSDA), which is well described in [23].

To begin the process, the incident energy of neutrons are binned and relayed for calculation of outgoing energy of the triton and alpha particle of Equation 8. The Q-value of the reaction is shown in Equation 9, where the incident energy of the neutron is added to the Q-value and then split between the outgoing alpha and triton - inversely proportional to the mass of the particle.

$$14.087 + 8.071 - 2.425 - 14.95 = 4.783 MeV \quad (9)$$

For an X-plane facing detector, the particle is then generated at a random location in the Y and Z directions and in the X direction based on Equation 10, or uniformly distributed for very thin materials. The particle is also assigned a randomly generated normal vector between -1 and 1 for the Y and Z coordinates and 0 and 1 for the X coordinate. The X coordinate is treated specially for this reaction because the triton and alpha are produced simultaneously in opposite directions. A coin-flip is used to decide which particle is transported in the positive X direction to save on computational time. The other particle is ignored since it will not enter the detector volume in this simplified model.

$$X = -\frac{ln(\xi)}{\Sigma} \quad (10)$$

where: Coordinate, X, Random number between 0 and 1, ξ, Macroscopic Cross Section, Σ

The range of the particle is calculated based on the properties of the generated particle and the collisional stopping power of the SiC detector volume based on Equation 11.

21

$$\frac{dE}{dx} = \frac{4\pi z^2 r_0^2 mc^2 N}{\beta^2} ln\left(\frac{2mc^2\beta^2}{I(1-\beta^2)} - \beta^2\right) \quad (11)$$

where: Collisional Stopping Power, $\frac{dE}{dx}$, Atomic number of incident particle, z, Classical electron radius, r_0, Electron rest mass, mc^2, Number density of the target material, N, Velocity of the particle relative to light, β, Mean excitation energy, I.

I is in turn defined by Equation 12:

$$I = \begin{cases} 19 & \text{if } Z = 1 \\ 11.2 + 11.7 * Z & \text{if } 2 \le Z \le 13 \\ 52.8 + 8.71 * Z & \text{if } Z > 13 \end{cases} \quad (12)$$

where: Atomic number of the target material, Z.

Finally, the Range of the particle can be calculated using Equation 13. The CSDA estimates a linear rate of energy deposition along the range of the charged particle. The length of the path contained within the active detector volume and outside the LiF conversion layer is used to calculate the energy of a count event and is visualized by Figure 22. A simulation of an arbitrary number of particles demonstrates the alpha and triton peaks originating from the LiF conversion layer (Figure 23).

$$Range = \frac{E}{\frac{dE}{dx}} \quad (13)$$

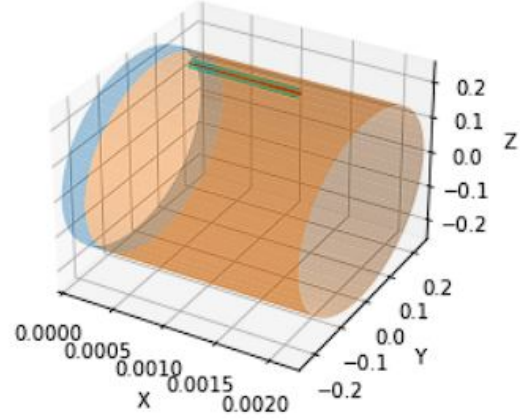where: Energy of incident neutron, E, Collisional Stopping Power, $\frac{dE}{dx}$.

Fig. 22. Range of a charged particle originating in the LiF layer (blue) into and out of the detector (orange), with particle path in red and energy deposition in green
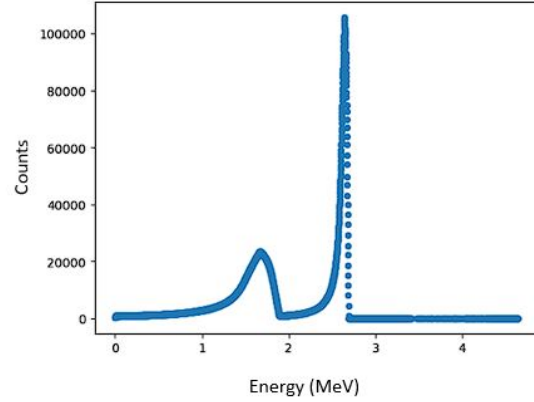

Fig. 23. Alpha and Triton peaks for a mono-energetic system

II.J. Heating

It is worth investigating the energy deposition rate upon the detector to ensure thermal

limits will not be exceeded. If natural convection is not enough to regulate detector temperature, a cooling system may need to be implemented. Equations for analysis are taken from [24]. Starting with the Biot number to get an idea of the temperature profile (Equation 14):

$$Biot = \frac{h * L_c}{k} \tag{14}$$

where: Heat transfer coefficient of the fluid, h, Characteristic Length, L_c, Thermal conductivity, k.

A quick order of magnitude analysis for the detector at the aforementioned "normal" dimensions has $L_c \approx$ 4E-4 m, h for air $\approx$ 10 W/m^{2}k, and k > 10 W/mk for all materials and gives a Biot number << 1. This suggests a uniform internal temperature distribution for the detector. Without energy generation, the energy storage is given by Equation 15.

$$E_{\text{storage}} = E_{\text{in}} - E_{\text{out}} \tag{15}$$

where: Energy, E.

The energy into the system is given by a heating tally and the energy out of the system is transferred via convection. The maximum temperature occurs when time $\to \infty$ and no more energy is stored. For a heating tally of around 2E16 eV/s or 3.07E-3 W (2 cm outside the RPV and at the core axial midplane, un-shielded) and

using Equation 16 for convection, one can solve for a T-T$_\infty$ of around 32.8 K. While only slight degradation is observed at temperatures of 500 °C [25], further analysis should be merited based on the support structure for the detector, the expected ambient temperature of the environment, and its ultimate size.

$$Q = hA(T - T_\infty) \tag{16}$$

where: Heat transfer rate, Q, Heat transfer coefficient of the fluid, h, Temperature of the object, T, Ambient temperature, T$_\infty$.

III. DISCUSSION

III.A. Detector Sensitivity

It has been demonstrated that the thermal neutron response of a SiC Schottky diode with LiF converter foil remains unchanged after fast neutron fluences up to 1.3E16 neutrons per cm^2 [25] and remains operable up to 1.7E17 neutrons per cm^2 [3]. The latter will serve as the hard limit for detector exposure. The minimum allowable sensitivity will be 2 counts per second. While operation at elevated temperatures and compensatory calibration have potential to extend the lifetime of a detector, the extent is currently unclear. A balance of position, size, and shielding will be necessary to allow for sufficient counts below the exposure limit.

The depletion rate of the Lithium-6 can be estimated based on the absorption rate in the LiF layer. The atom density of the Li-6 is around 1.08E24 atoms per cc. Taking 1% change in the atom density as the limit for depletion, the number of absorption events required to hit this limit will occur after the total neutron fluence limit.

III.B. Conversion Layer

Optimization in the conversion layer is based on the trade off between thickness allowing for a greater interaction chance while increasing the path length required to reach the detector volume. Reaction rate tallies for absorption in the LiF volume from SCALE were fed into the previously mentioned python script for charged particle transport to determine a max theoretical count rate for the detector. This serves as an indicator of detection efficiency and can be used to estimate the optimal thickness of the LiF layer. The data was fit (Figure 24) using a two-term exponential in the form of Equation 17. A summary of the tuned parameters and optimized thickness is found in Table VI.

$$f(x) = a \exp(bx) + c \exp(dx) \qquad (17)$$

where: Parameters, a, b, c, d.

The observed optimal thickness of 28.33 microns for a lower level discrimination of 300 keV agrees fairly well with the findings of [26,27], but may be further tuned depending on desired levels of discrimination. It is also important to note that the energy resolution decreases rapidly as the thickness of the converter layer increases, as can be seen in the difference between spectrums for 0.5 and 10 micron thick layers (Figure 25).

III.C. Location

From Figure 7, fast fluence can be seen to range from about 5E10 to 1E11 neutrons per cm^2-s in the region between the reactor core and the neutron shield. It is not until a point within the neutron shield that fluxes are low enough (about 1E9 neutrons per cm^2-s) to allow for a 5 year detector lifetime. While the behavior of a detector relative to a plane, line, or point source is well understood, the detector can be modeled at several radial locations about the core center to obtain a general trend in tally data. A set of simulations was carried out with the neutron shield and reactor enclosure removed to extend the range of data available as only a function of distance. This doubles to illustrate the effect of the neutron shield as a reflector and may be compared with Figure 7. Distance vs. Flux is shown in Figure 26(a), while Distance vs. Counts is shown in Figure 26. Care

TABLE VI
Summary of fit properties

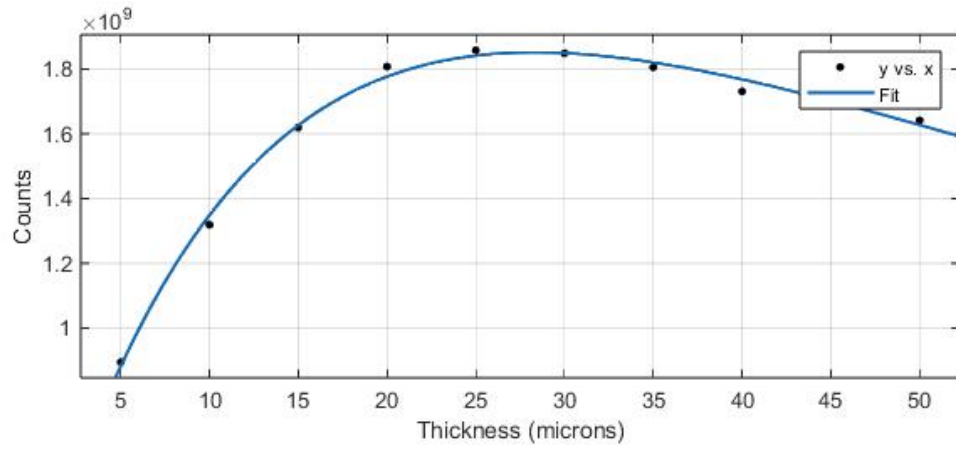| a	b	c	d	Optimal Thickness (microns)
3.135E09	-0.01224	-2.997E09	-0.07431	28.33

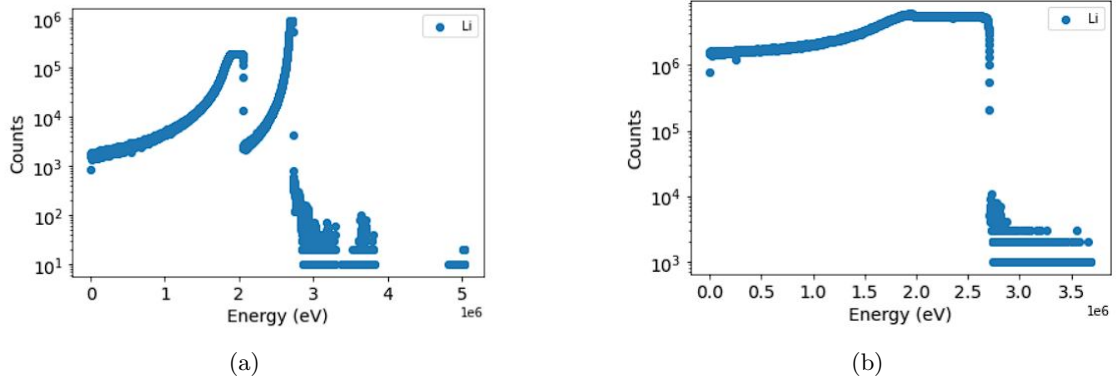Fig. 24. Converter layer Thickness vs Counts

(a)

(b)

Fig. 25. Comparison of energy spectra for (a) 0.5 and (b) 10 micron thick LiF layers

should be taken if locating a detector next to a material interface since the fits do not accurately characterize albedo effects. The drastic difference between counts relative to flux without the Neutron Shield implies the spectrum becomes faster. Indeed, when looking at flux profiles (Figure 26(c), Figure 26(d)), it can be seen that the Neutron Shield creates a more thermal spectrum. The location based datasets therefore have very limited application as they are very dependent on the location and size of the Neutron Shield.

III.D. Shielding

Some level of shielding is required to reduce the exposure of the detector and thereby extend its lifetime. Varied thicknesses of a Boron Carbide cylinder encasing the detector are simulated to assess the impact of shielding. It is acknowledged that the B-10 thermal capture reaction will also generate a 1.47 or 1.78 MeV alpha particle which could impinge on the detectors active volume. The intent is to investigate the amount of shielding necessary rather than a comprehensive analysis of shielding materials. Results for varied shielding thickness are shown in Figure 27. The trend for flux is seen to agree somewhat with a predicted value using the half-value thickness of Boron Carbide reported in [28]. This does not translate directly to count observations, however, because the flux profile incident on the detector also changes as a result of the shielding and the drop in counts with shielding is rapid.

If instead, polyethylene is used as the shielding material, it will scatter the neutrons rather than absorb the thermal neutrons which would otherwise be more likely to interact in the LiF layer. This would allow for higher count rates, while achieving the same reduction in flux. The change in flux and counts is not monotonic for the polyethylene and requires a greater thickness than B4C to reduce flux by the same amount (Table VIII).

III.E. Size

To vary the size of SiC detection systems, it is most typical to create arrays of SiC detectors. For thermal neutron detection, the length of the active volume is only relevant so far as to trap the tritons and alphas produced in the conversion layer. The cross sectional area is therefore modified to observe the effect on count rate. For a constant flux, the number of counts is seen to increase linearly (Equation 18) with area as shown in Figure 28.

TABLE VII
Summary of fit properties

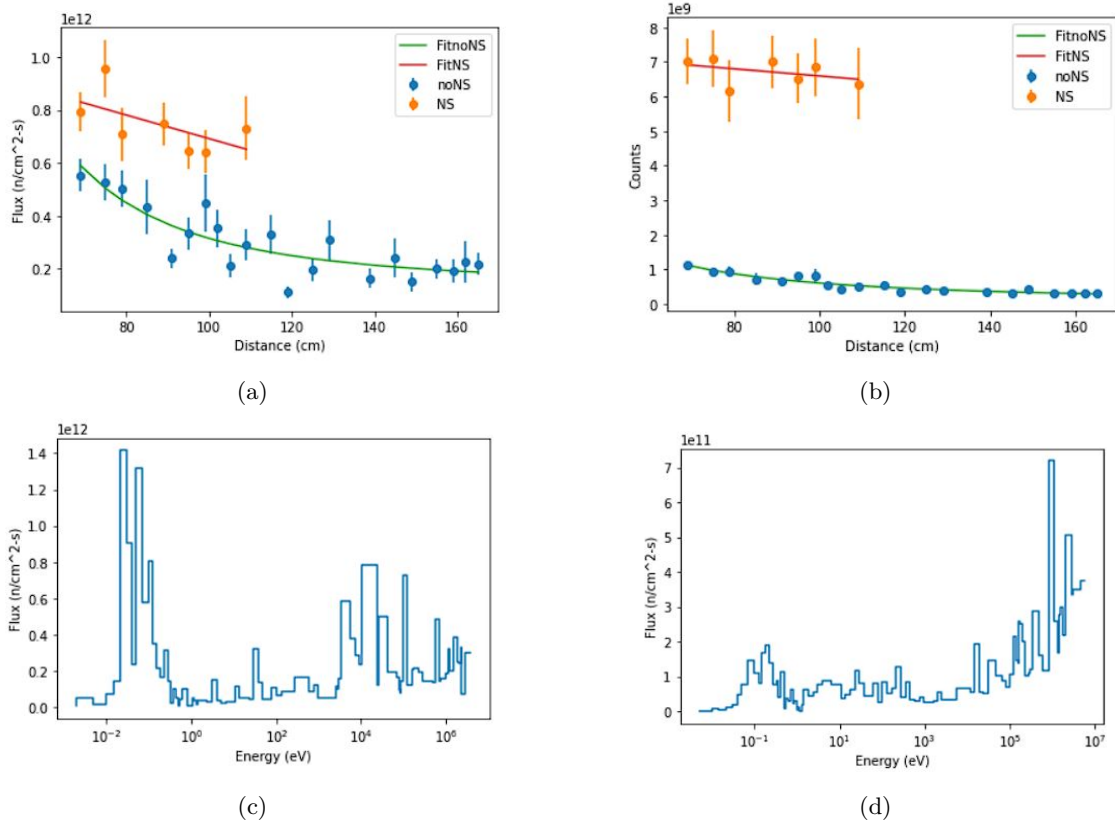| FluxNS	$Flux = (-4.446E09) * x + 1.136E12$
FluxnoNS	$Flux = 1.839E16 * x^{-2.507} + 1.373E11$
CountsNS	$Counts = (-1.039E07) * x + 7.634E09$
CountsnoNS	$Counts = (2.618E12) * x^{-1.85} + 8.27E07$

(a)

(b)

(c)

(d)

Fig. 26. (a) Flux and (b) Counts vs. Distance. The flux profile at 75 cm is shown to be more thermal (c) with the Neutron Shield/Reactor Enclosure than (d) without.

TABLE VIII
Summary of fit properties

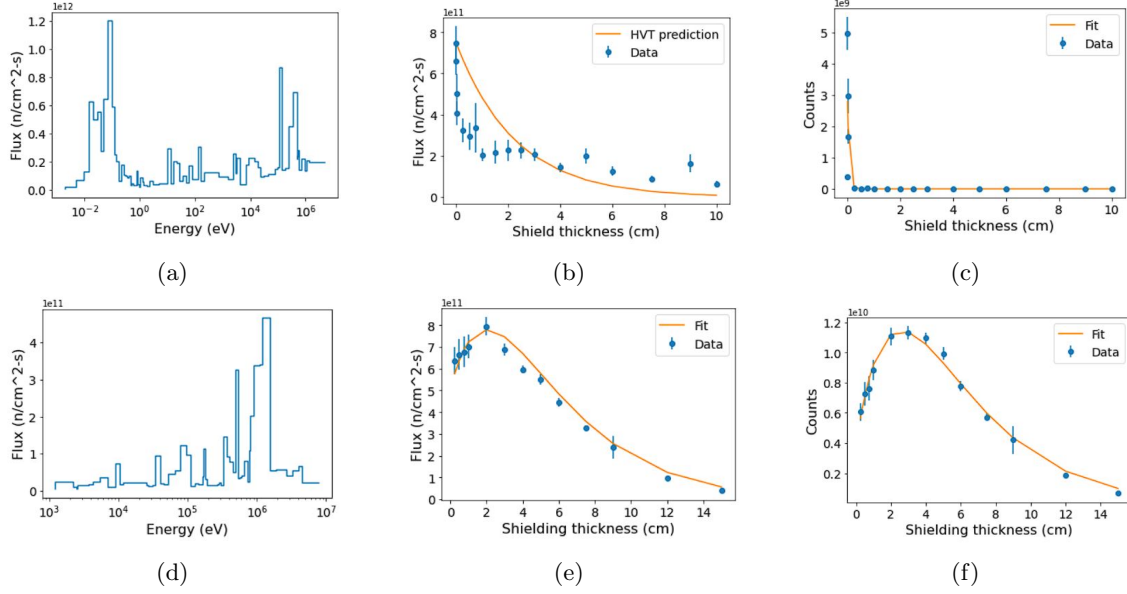| Predicted Flux (B4C)	$Flux = 7.48E11 * 0.5^{thickness/1.575}$
Counts (B4C)	$Counts = 2.801E09 * e^{-16.47*x}$
Flux fit (Poly)	$Flux = 7.234E14 * e^{-.3311*x} + -7.229E14 * e^{-0.3318*x}$
Counts (Poly)	$Counts = -3.177E11 * e^{-0.3429*x} + 3.216e + 11 * e^{-0.3152*x}$

(a)

(b)

(c)

(d)

(e)

(f)

Fig. 27. The flux profile for (a) no shielding vs. (d) 5 cm of B4C highlights a loss of thermal neutron population with shielding. Flux and theoretical counts vs. shield thickness size are shown for B4C (b & c) and poly (e & f).
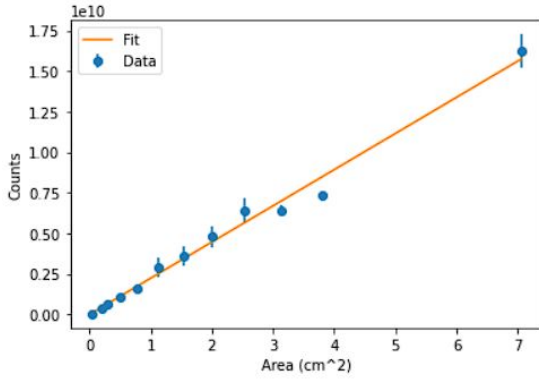

Fig. 28. Cross Sectional Area vs max Counts

$$Counts = 2.229E9 * Area + 7.868E6 \qquad (18)$$

III.F. Solving for the Optimal Specifications

A simple approach is to use the existing infrastructure and place the detector behind the Neutron Shield to remain below the lifetime fluence limit. A detector of r=0.2481 cm, located at 139 cm yields the following at full power (Figure 29(a)), and when shutdown Figure 29(b)). While in the power-range, the prompt neutron-induced gamma flux is significantly greater than the gamma flux from material inventory, and is therefore proportional to core-power [3]. This location is therefore sufficient at full power, but the decayed primary source signal is not large enough to generate counts in the detector via Li conversion. This remains true even when the detector radius is increased to 25 cm Figure 29(c), though 3 counts from direct neutron absorption are observed in the active volume making that a possible strategy.
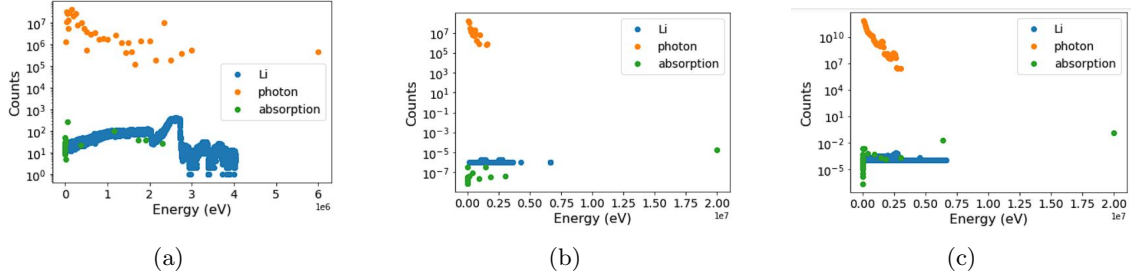
Fig. 29. A detector located behind the Neutron Shield at (a) full power, (b) in the source range, and (c) in the source range for a radius increased to 25 cm.

Alternatively, one can start with an unshielded detector at 69 cm and use the developed fit equations to adjust specifications until the maximum fluence and minimum count rate are obtained. In Figure 30, around 6 counts can be discriminated from the gamma signal. In the power range, the flux would be around 7.94E11 n/cm^2-s. First maxing out distance to 123 cm, flux decreases to 5.89E11 and the count rate should decrease by around 9%. The remainder of the decrease, however, would need to come from 11 cm of B4C shielding, making it impossible to obtain any counts originating from the Li conversion based on the equation in Table VIII.
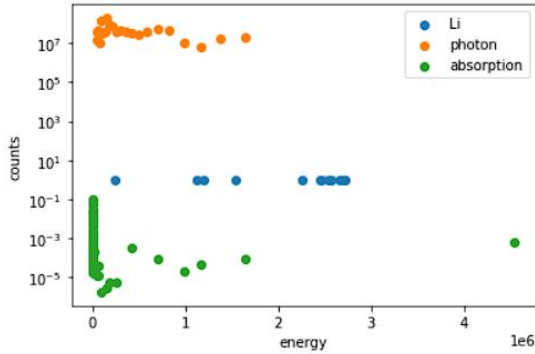

Fig. 30. Source range detection (.2481cm radius, 69cm away from core midpoint)

Switching to polyethylene, a standing shield of minimum required dimension allows for enough LiF conversions to occur at a reasonable detector size, but the photon energies exceed the triton energy range (Figure 31(a)). Discrimination would then need to rely on direct absorption events above about 4 MeV. This is also not very practical since the count rate here is only around 0.057 counts a second, requiring at least a 35 times larger detector (175 cm radius).

From Figure 29(c), two more test cases can be proposed of a B4C shield for reliance on direct absorptions inside the NS, or reordering the NS to B4C followed by poly to perhaps thermalize the faster neutrons that make it through the B4C layer and allow for more counts. Results for the first option are shown in Figure 31(b), where a radius of about 10 cm is required to obtain 2 cps. Reversing the NS to be an absorbing media followed by a scattering media suffers from the same issue as poly on its own (Figure 31(a)).

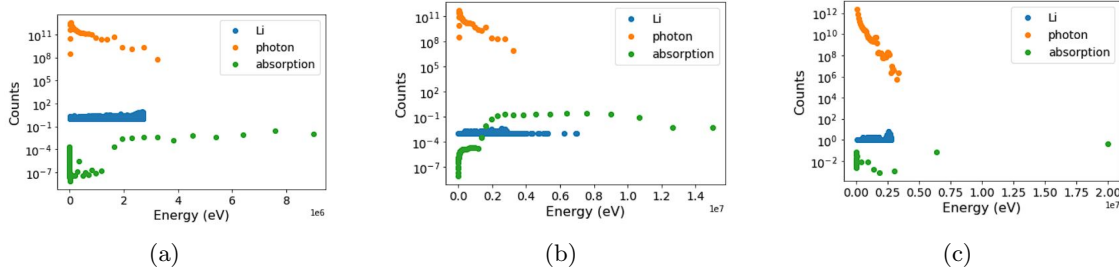These examples show that for the current

Fig. 31. Source range detection. (a) 5cm radius detector, 20cm of poly shielding, 89cm from core midpoint. (b) 10cm radius detector, 12cm of B4C shielding, 89cm from core midpoint. (c) 25 cm radius detector, located behind a reversed Neutron Shield.

experimentally demonstrated lifetimes of SiC detectors, it would be necessary to either have a removable shield or a large detector relying on direct absorption to allow for monitoring in the source range (Figure 32). At 6 counts/sec, however, the area of an un-shielded detector could decrease by a factor of 3 relative to the 0.193 cm^2 (r=.2481 cm) and still remain sufficiently large (Figure 33).

IV. CONCLUSIONS

The reactor environment around a simple Molten Salt Reactor design was investigated using SCALE and OpenMC for the purpose of using ex-core SiC detection systems. Strong agreement was found between the 2 codes for criticality and depletion simulations, but the lack of automated variance reduction for OpenMC made it difficult to perform sensitivity studies on the small detector volume for comparison with MAVRIC. Multiple configurations were analyzed to appropriately bound the worst case re-

actor environments; the mild burnup of the core meant BOL served as the highest magnitude flux environment for the upper bound, while a primary source was added in a sub-critical configuration to simulate a source range environment. The change in fluxes from 0 days to 180 days after shutdown was also found to be minimal.

As far as the detector itself, multiple observations were made:

1. Nuclear heating can be expected to raise the temperature of the detector by about 33K relative to the ambient temperature.

2. The optimal thickness of a LiF converter layer is around 28 microns, but energy resolution suffers rapidly after only a few microns.

3. The location of the detector within air volumes has a mild linear influence on count rate.

4. Shielding has a dramatic impact on the count rate due to the added effect of change the neutron energy spectrum.
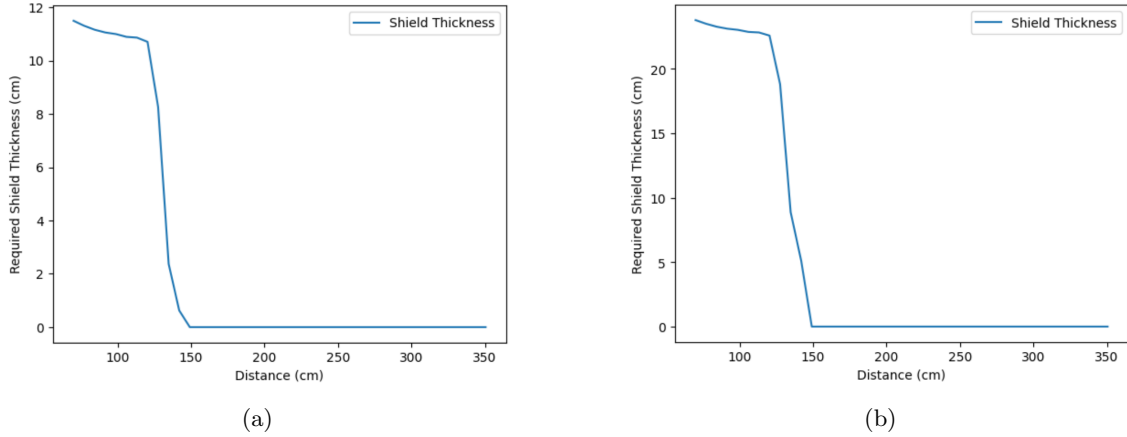
(a)

(b)

Fig. 32. Minimum shielding thickness to remain below the fluence requirement as a function of distance for (a) B4C and (b) poly.

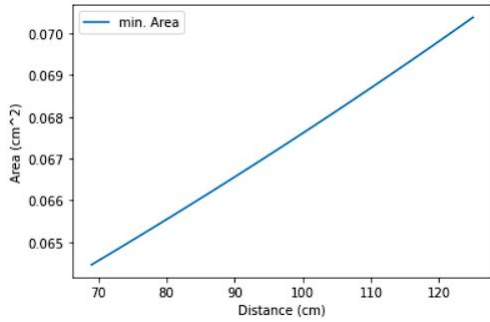5. Count rate has an intuitive linear correlation with the area of the detector.

Fig. 33. Minimum area to get 2 counts per second in the source range for an unshielded detector.

Using a SiC detector in a Molten Salt Reactor environment therefore has a few viable strategies. A removable absorbing shield would allow for operation within the Neutron Shield in both the power and source ranges. It may be possible to rely directly on absorption reactions in the active SiC volume rather than the LiF layer for source range measurements using relatively large detectors and sufficient B4C shield-ing. Inside the neutron shield this would equate to about 12 cm of B4C shielding with a roughly 10 cm radius detector, while outside the neutron shield would require an around 25 cm radius. Lastly, if the lifetime of the SiC detector reaches the 1E19-1E20 total neutron fluence level of commercially available ion chambers, excore implementation becomes rather trivial.

V.   ACKNOWLEDGMENTS

31

REFERENCES

[1] J. M. HARRER and J. G. BECKER-LEY, "Nuclear power reactor instrumentation systems handbook. Volume 2," (1974); 10.2172/4312290., URL https://www.osti.gov/biblio/4312290.

[2] "Westinghouse Technology Systems Manual Section 9.1 Excore Nuclear Instrumentation," (2016).

[3] F. H. RUDDY, A. R. DULLOO, J. G. SEIDEL, F. W. HANTZ, and L. R. GROBMYER, "Nuclear Reactor Power Monitoring Using Silicon Carbide Semiconductor Radiation Detectors," *Nuclear Technology*, **140**, *2*, 198 (2002).

[4] B. PETROVIĆ, F. H. RUDDY, and C. LOMBARDI, "Optimum strategy for ex-core dosimeters/monitors in the iris reactor," *Reactor Dosimetry in the 21st Century*, 43–50, World Scientific.

[5] B. PETROVIC and T. FLASPOEHLER, "Feasibility of Ex-Core In-Vessel Nuclear Instrumentation for Integral Inherently Safe Light Water Reactor (I2S-LWR)," *2015 International Conference on Applications of Nuclear Techniques, Crete, Greece* (2015).

[6] T. FLASPOEHLER and B. PETROVIC, "Radiation environment in the I2S-LWR concept: Part I–Radial distribution and its impact on vessel fluence, neutron detectors placement, and radial reflector gamma heating," *Annals of Nuclear Energy*, **145**, 106272 (2020).

[7] "Abilene Christian University Molten Salt Research Reactor Preliminary Safety Analysis Report, Revision 0," (2022).

[8] M. ROSENTHAL, P. KASTEN, and R. BRIGGS, "Molten-salt reactors—history, status, and potential," *Nuclear Applications and Technology*, **8**, *2*, 107 (1970).

[9] "Chapter 2 - Generation IV International Forum (GIF)," I. L. PIORO (Editor), *Handbook of Generation IV Nuclear Reactors (Second Edition)*, Woodhead Publishing Series in Energy, 111–132, Woodhead Publishing; https://doi.org/10.1016/B978-0-12-820588-4.00010-4.

[10] R. C. ROBERTSON, "MSRE Design & Operations Report Part 1 Description of Reactor Design," , Oak Ridge National Lab.(ORNL), Oak Ridge, TN (United States) (1965).

[11] D. E. HOLCOMB, R. A. KISNER, and S. M. CETINER, "Instrumentation framework for molten salt reactors," , Oak Ridge National Lab.(ORNL), Oak Ridge, TN (United States) (2018).

[12] M. De Napoli, "SiC detectors: A review on the use of silicon carbide as radiation detection material," *Frontiers in Physics*, **10** (2022); 10.3389/fphy.2022.898833., URL `https://www.frontiersin.org/articles/10.3389/fphy.2022.898833`.

[13] T. Yang, Y. Tan, Q. Liu, S. Xiao, K. Liu, J. Zhang, R. Kiuchi, M. Zhao, X. Zhang, C. Wang, B. Wu, J. Lin, W. Song, H. Lu, and X. Shi, "Time Resolution of the 4H-SiC PIN Detector," *Frontiers in Physics*, **10** (2022); 10.3389/fphy.2022.718071., URL `https://www.frontiersin.org/articles/10.3389/fphy.2022.718071`.

[14] F. Nava, G. Bertuccio, A. Cavallini, and E. Vittone, "Silicon carbide and its use as a radiation detector material," *Measurement Science and Technology*, **19**, *10*, 102001 (2008); 10.1088/0957-0233/19/10/102001., URL `https://dx.doi.org/10.1088/0957-0233/19/10/102001`.

[15] W. A. Wieselquist, R. A. Lefebvre, and M. A. Jessee, Eds., "SCALE Code System," , ORNL/TM-2005/39, Version 6.2.4, Oak Ridge National Laboratory, Oak Ridge, TN (2022).

[16] P. K. Romano, N. E. Horelik, B. R. Herman, A. G. Nelson, B. Forget, and K. Smith, "OpenMC: A state-of-the-art Monte Carlo code for research and development," *Annals of Nuclear Energy*, **82**, 90 (2015); https://doi.org/10.1016/j.anucene.2014.07.048., URL `https://www.sciencedirect.com/science/article/pii/S030645491400379X`, joint International Conference on Supercomputing in Nuclear Applications and Monte Carlo 2013, SNA + MC 2013. Pluri- and Trans-disciplinarity, Towards New Modeling and Numerical Simulation Paradigms.

[17] R. J. McConn, C. J. Gesh, R. T. Pagh, R. A. Rucker, and R. Williams III, "Compendium of material composition data for radiation transport modeling," , Pacific Northwest National Lab.(PNNL), Richland, WA (United States) (2011).

[18] M. Pusa and J. Leppänen, "Computing the Matrix Exponential in Burnup Calculations," *Nuclear Science and Engineering*, **164**, *2*, 140 (2010); 10.13182/NSE09-14., URL `https://doi.org/10.13182/NSE09-14`.

[19] M. Pusa, "Rational Approximations to the Matrix Exponential in Burnup Cal-

culations," *Nuclear Science and Engineering*, **169**, *2*, 155 (2011); 10.13182/NSE10-81., URL `https://doi.org/10.13182/NSE10-81`.

[20] "Westinghouse Technology Systems Manual," (2016).

[21] F. FRANCESCHINI, F. H. RUDDY, and B. PETROVIĆ, "Simulation of the response of silicon carbide fast neutron detectors," *Reactor Dosimetry State of the Art 2008*, 128–135, World Scientific.

[22] TRKOV, ANDRE AND BROWN, DAVID A, "ENDF-6 formats manual: data formats and procedures for the evaluated nuclear data files," , Brookhaven National Lab.(BNL), Upton, NY (United States) (2018).

[23] J. E. TURNER, *Atoms, radiation, and radiation protection*, John Wiley & Sons (2008).

[24] A. FAKHERI, *Intermediate Heat Transfer*, Taylor & Francis (2013).

[25] F. H. RUDDY, L. OTTAVIANI, A. LYOUSSI, C. DESTOUCHES, O. PALAIS, and C. REYNARD-CARETTE, "Silicon Carbide Neutron Detectors for Harsh Nuclear Environments: A Review of the State of the Art," *IEEE Transactions on Nuclear Science*, **69**, *4*, 792 (2022); 10.1109/TNS.2022.3144125.

[26] D. MCGREGOR, M. HAMMIG, Y.-H. YANG, H. GERSCH, and R. KLANN, "Design considerations for thin film coated semiconductor thermal neutron detectors—I: basics regarding alpha particle emitting neutron reactive films," *Nuclear Instruments and Methods in Physics Research Section A: Accelerators, Spectrometers, Detectors and Associated Equipment*, **500**, *1*, 272 (2003); https://doi.org/10.1016/S0168-9002(02)02078-8., URL `https://www.sciencedirect.com/science/article/pii/S0168900202020788`, nIMA Vol 500.

[27] Z. ZHANG and M. D. ASPINALL, "Comparison of Neutron Detection Performance of Four Thin-Film Semiconductor Neutron Detectors Based on Geant4," *Sensors*, **21**, *23* (2021); 10.3390/s21237930.

[28] B. BUYUK and A. B. TUGRUL, "Gamma and neutron attenuation behaviours of boron carbide–silicon carbide composites," *Annals of Nuclear Energy*, **71**, 46 (2014); https://doi.org/10.1016/j.anucene.2014.03.026., URL `https://www.sciencedirect.com/science/article/pii/S0306454914001480`.